

IUTAM Symposium Wind Waves, 4-8 September 2017, London, UK

Simulation-based study of wind-wave interaction

Xuanting Hao^a, Tao Cao^a, Zixuan Yang^a, Tianyi Li^a, Lian Shen^{a,*}

^aDepartment of Mechanical Engineering and St. Anthony Falls Laboratory, University of Minnesota, Minneapolis, 55455, United States

Abstract

We use a suite of advanced numerical tools developed in house to investigate the physical processes in three canonical wind–wave interaction problems. First, we use DNS to investigate the sheltering effect of a long wave on a short wave. It is found that in the presence of the long wave the form drag of the short wave decreases, with the magnitude of the reduction depending on the wave age of the long wave. We also observe that the surface friction is highly correlated to the streamwise vorticity upstream. Next, we study the effect of wave breaking on the wind turbulence. We focus on analyzing small-scale flow physics near the wave surface and the influence of wave breaking on turbulence statistics. It is found that plunging breakers induce acceleration of the air flow near the wave surface. During wave plunging, a large spanwise vortex is generated, which enhances the turbulence mixing around it, and induces large magnitude of turbulent kinetic energy. In the final part, results are presented for wind over broad-band waves in realistic ocean settings. By examining the full wavenumber–frequency spectrum of the turbulent wind, we have identified distinct wave signatures in the space–time correlation of wind turbulence. In the evolution of the wave field, its inner physical process known as the four-wave interaction dominates over wind input, as shown in the frequency downshift phenomenon of the wave field throughout the numerical experiments.

© 2018 The Authors. Published by Elsevier B.V.

Peer-review under responsibility of the scientific committee of the IUTAM Symposium Wind Waves.

Keywords: wind-wave interactions; air-sea interactions; atmospheric boundary layer; geophysical turbulence; free surface flow; wave breaking; nonlinear resonant interactions

1. Introduction

Wind–wave interactions play an important role in the energy and momentum transfer between the marine atmospheric boundary layer and upper oceans. Understanding the wind–wave interaction process is crucial for a number of fundamental scientific studies and engineering applications. However, the complexity of the wind–wave system, particularly that caused by the irregular wave surface and wave breaking, brings significant challenges to the numerical study of wind–wave interactions. With the growth in computing power and the advancements in numerical algorithms, computer simulation has been playing an increasingly important role in the study of wind–wave interactions. Using methods including a high-order spectral (HOS) method for nonlinear waves, direct numerical simulation (DNS) and large-eddy simulation (LES) of wind turbulence on wave-surface-fitted grid, and the coupled level-set and

* Corresponding author.

E-mail address: shen@umn.edu

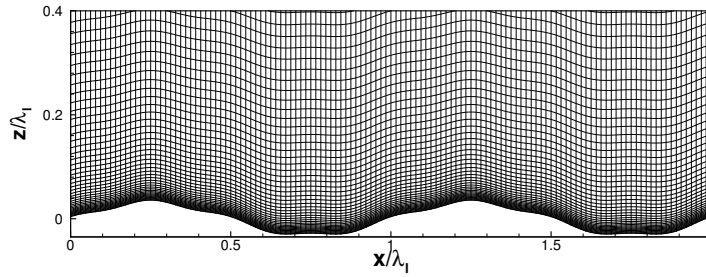


Fig. 1. The grid structure of DNS over two waves.

volume-of-fluid method for breaking waves, we have developed an advanced computational framework for wind–wave interaction called the WOW (Wave–Ocean–Wave). Using the tool of WOW, we have studied different aspects of wind–wave interaction, including wind over two progressive waves, wind over breaking waves, and wind over broad-band waves.

2. Wind over Two Progressive Waves

2.1. Cases description

Table 1. List of case parameters in the DNS of wind turbulence over a long wave and a short wave.

Case	c_l/u_*	c_s/u_*	λ_l/λ_s	$(ak)_l$	$(ak)_s$	$Re = u_* \lambda_l/\nu$
W02	2	1	4	0.2	0.1	283
W14	14	7	4	0.2	0.1	283
W25	25	12.5	4	0.2	0.1	283

In this session, we perform a DNS study of wind over two progressive water waves. The bottom of the simulation domain is the superposition of two linear water waves, including a long wave with wavelength λ_l and a short wave with wavelength λ_s , with a wavelength ratio $\lambda_l/\lambda_s = 4$. The ratio of the phase speed and amplitude between the long wave and short wave can be determined from the wavelength ratio based on the power law of broad-band wave field:

$$c_l/c_s = (\lambda_l/\lambda_s)^{\frac{1}{2}} = 2 \quad a_l/a_s = (\lambda_l/\lambda_s)^{\frac{3}{2}} = 8 \quad (1)$$

where c_l , c_s are the phase speeds of the long wave and short wave, respectively; a_l , a_s are respectively the amplitudes of the long wave and short wave. In the problem setup, the wave steepness of long wave $(ak)_l$ is set to 0.2. We have studied three wave ages of the long wave, $c_l/u_* = 2$, 14, and 25, corresponding to slow wave case W02, intermediate wave case W14, and fast wave case W25, respectively. The wave age and wave steepness of the short waves are obtained based on equation 1. The surface elevation η is prescribed at each time step in the simulation as

$$\eta = a_l \sin k_l(x - c_l t) + a_s \sin k_s(x - c_s t) \quad (2)$$

We use x , y , and z to denote the streamwise, spanwise, and vertical coordinates, respectively, and u , v , and w to represent the velocity component in each direction. The size of the computational domain is $4\lambda_l$, $3\lambda_l$, and $2\lambda_l$ in x , y , and z directions, respectively, discretized with $256 \times 128 \times 129$ grid points which are evenly spaced in the horizontal plane and stretched in the vertical direction as shown in figure 1. The parameters are summarized in Table 1 and the numerical details and validations can be found in [1] and [2].

2.2. Sheltering effect

The suppress of the growth rate of short waves by the presence of long waves has been reported in literature [3, 4, 5]. However, more research is needed to reveal the underlying mechanism. In the present study, we aim to investigate the

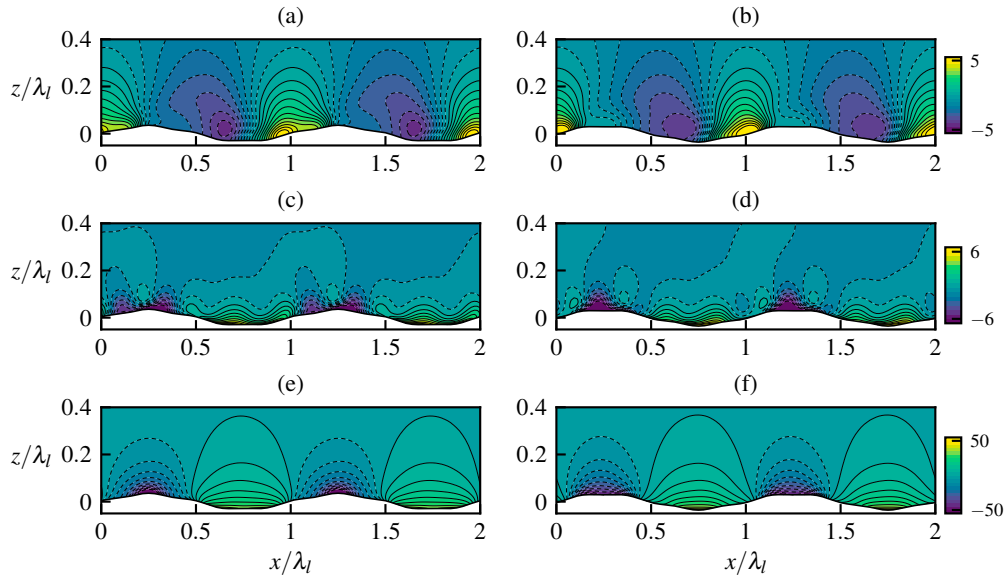


Fig. 2. Contours of phase-averaged pressure with conditional averaging under the crest condition and trough condition at different wave ages. (a) W02C; (b) W02T; (c) W14C; (d) W14T; (e) W25C; (f) W25T.

sheltering effect of long waves with various wave ages on the short waves. To obtain statistics of the turbulence field over two surface waves, we perform conditional averaging, including: (a) a crest condition where the crest of the long wave and that of the short wave coincide, which is indicated by the suffix “C”, and (b) a trough condition where the crest of the long wave and the trough of the short wave coincide, which is indicated by the suffix “T”. We use W02C, W14C, and W25C to denote the conditional averages of case W02, W14, and W25 respectively, based on the crest condition; and W02T, W14T, and W25T to represent conditional averages based on the trough condition.

Fig. 2 (a, b) shows the phase-averaged pressure field for $c_l/u_* = 2$, (c, d) for $c_l/u_* = 14$, and (e, f) for $c_l/u_* = 25$, corresponding to the slow, intermediate, and fast wave cases, respectively. The signature of short waves on the flow field can be seen from the variation of the spatial distribution of the maxima and minima of the pressure between the two types of conditionally averaged cases for each wave age. For the slow wave case W02, the positive pressure peak is where the windward side of the long wave coincides with that of the short wave, at $x/\lambda_l < 1$ for the conditionally averaged case W02C and at $x/\lambda_l > 1$ for case W02T; for the intermediate wave case W14, there are two peaks of pressure near the crest of the long wave in the conditionally averaged case W14C, while only one negative peak for case W14T; for the fast wave case W25, the difference is less obvious because the pressure distribution is more symmetric.

Table 2. Values of form drag in different cases.

Case	Form drag	Two-wave	Long-wave-only	Short-wave-only
$c_l/u_* = 2$	$F_{pl} + F_{ps}$	0.3646	0.3277	0.0398
	F_{pl}	0.3488	0.3277	–
	F_{ps}	0.0158	–	0.0398
$c_l/u_* = 14$	$F_{pl} + F_{ps}$	0.0360	0.0022	0.0714
	F_{pl}	–0.0189	0.0022	–
	F_{ps}	0.0550	–	0.0714
$c_l/u_* = 25$	$F_{pl} + F_{ps}$	–0.1423	–0.1275	–0.0206
	F_{pl}	–0.1292	–0.1275	–
	F_{ps}	–0.0140	–	–0.0206

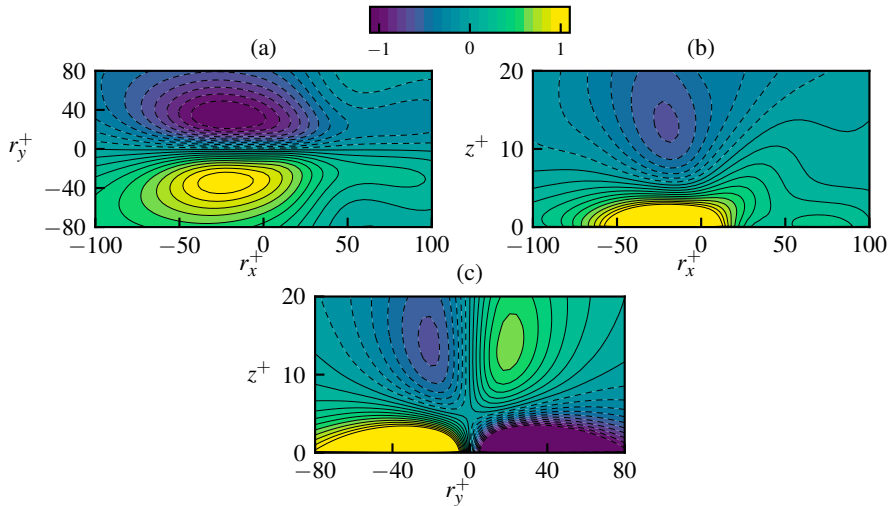


Fig. 3. Contours of the correlation function of the surface friction and streamwise vorticity at different planes: (a) $(z - \eta)^+ = 3.3$; (b) $r_y^+ = -17$; (c) $r_x^+ = -22$.

Next, we analyze the form drag on the surface waves. We decompose the total form drag on the wave surface in the two-wave cases into two parts, namely F_{pl} , which is the form drag acting on the long wave, and F_{ps} , which is the form drag on the short wave. The results are shown in Table 2. For comparison, we also include the form drag on the long waves and short waves, respectively in the long-wave-only cases and short-wave-only cases listed in Table 2. As shown, compared with the short-wave-only cases, the form drag on the short waves is reduced significantly in the presence of the long waves. On the other hand, the form drag on the long waves does not vary much between the two-wave cases and long-wave-only cases.

In Table 3, we calculate the reduction of the form drag on the short waves in the two-wave cases compared with the short-wave-only cases. As shown, the reduction is significant, with the relative magnitude depending on the wave age of the long waves, which is associated with the form drag on the long waves. In the slow wave case, in which the magnitude of F_{pl} is the largest, the reduction in F_{ps} is the most; in the fast wave case, both F_{pl} and F_{ps} are negative, and the magnitude of F_{ps} is also reduced by the presence of the long wave; in the intermediate wave case, the reduction of F_{ps} is the smallest, while the magnitude of the form drag on the long wave is also the lowest.

Table 3. Reduction of form drag on the short wave due to the presence of the long wave, and values of form drag on the long waves.

c_l/u_*	2	14	25
$ \Delta F_{ps}/F_{ps} $	60%	22%	32%
F_{pl}	0.3488	-0.0189	-0.1292

2.3. Correlation between surface friction and streamwise vorticity

In the slow wave case with $c_l/u_* = 2$, we observe that the total form drag in the two-wave case is larger than that in the long-wave-only case. Because the summation of the form drag and viscous drag on the surface is constant in the problem setup, i.e. u_* is kept the same, an increase in the form drag corresponds to a decrease in the friction drag. Our DNS data show that the viscous drag is mainly concentrated on the windward of the long wave both in the two-wave case and the long-wave-only case.

It is found that the reduction of surface friction is related to the vortical structures in wind turbulence. This can be demonstrated using the correlation function of the streamwise vorticity and surface friction defined as

$$R(r_x, r_y, z) = \overline{\tau_S(x, y, 0)\omega_x(x + r_x, y + r_y, z)/(u_*^4/\nu)} \quad (3)$$

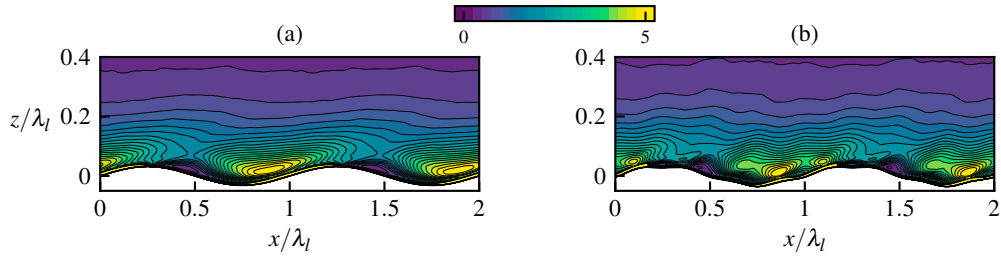


Fig. 4. Contours of phase-averaged enstrophy $\langle \omega_x \omega_x \rangle$ for $c_l/u_* = 2$. (a) long-wave-only case; (b) two-wave case W02T.

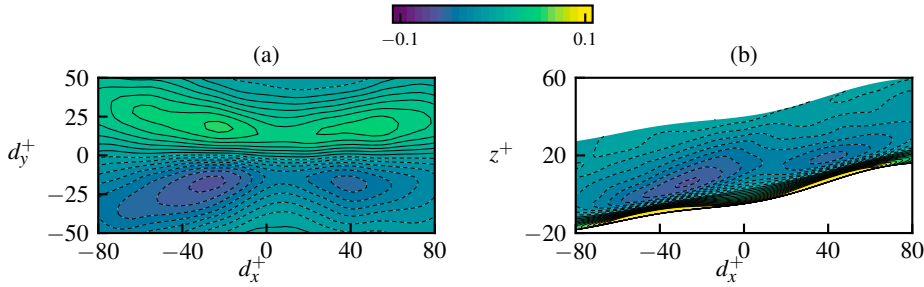


Fig. 5. Contours of conditionally averaged streamwise vorticity. (a) $(z - \eta)^+ = 15$; (b) $d_y^+ = -18$.

where $\omega_x = \partial w / \partial y - \partial v / \partial z$ is the streamwise vorticity, τ_s is surface friction, and r_x and r_y are spatial separations in x and y directions, respectively. The $R(r_x, r_y, z)$ was used in [6] to study the correlation between the friction and streamwise vorticity in channel flows. It was found that in channel flows, the friction is mainly induced by the streamwise vortices. For the present problem of wind turbulence over waves, Fig. 3 illustrates R in case W02T, which is averaged on the windward face of the long wave. As shown in Fig. 3(a) and (c), R has an anti-symmetric distribution with respect to r_y . Fig. 3(a) and (b) shows that R reaches its peak at $r_x^+ \approx -22$, indicating that the surface friction at the wave surface is mainly correlated to the upstream near-wall vorticity, in contrast to the channel flow where the surface friction is mostly correlated to downstream vorticity [6].

Fig. 4 shows the spatial distribution of phase-averaged enstrophy $\langle \omega_x \omega_x \rangle$ for $c_l/u_* = 2$ in the long-wave-only case and two-wave case. A comparison between these two cases indicates that the high concentration of enstrophy at the windward side of the long wave in case W02T is broken at the position $x/\lambda_l = 1$ by the presence of the short wave. Also, at this position, it is found that the surface friction is significantly reduced compared with the long-wave-only case (result not plotted here due to space limitation).

The correlation between the streamwise vortical structure and surface friction can also be shown through conditional average, which extracts the coherent structure related to the surface friction by the following criterion [6]

$$\tau_S(x_0, y) > \alpha \langle \tau_S \rangle(x_0) \quad (4)$$

where τ_S represents the surface friction, $\langle \rangle$ denotes the phase average, α is a threshold and equals 2 in the present study, and x_0 is the position of the conditional average. We perform the conditional average at the position $x_0/\lambda_l = 1$ based on equation 4, the result of which is plotted in Fig. 5. As shown, the conditionally averaged ω_x field recovers the “broken” structure of the streamwise vorticity shown in Fig. 4, in which there are peaks of streamwise vorticity both at the upstream and downstream of the detection point.

3. Wind over Breaking Waves

Wave breaking plays an important role in air–sea interactions, which influence the sea states and marine atmospheric boundary layer. It has been summarized in many review papers [7, 8, 9, 10, 11, 12] that due to wave breaking, turbulence, vorticity, and ocean currents are generated, and the mass, momentum, and energy transfer between the

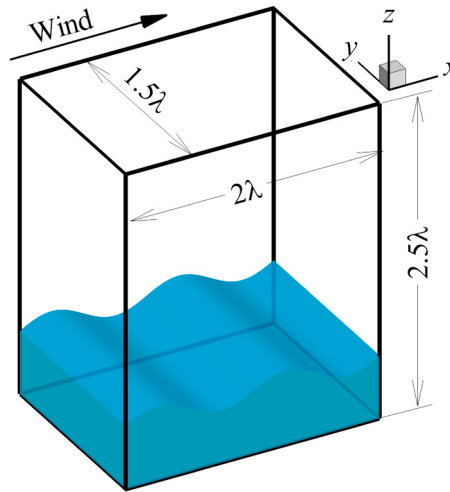


Fig. 6. Computational domain and coordinate system for DNS of wind over breaking waves.

atmosphere and oceans is enhanced. It would be helpful to investigate wind turbulence over breaking waves for improving ocean–atmosphere interaction models.

Wind over breaking waves has been studied in laboratory experiments and field measurements. Although numerical simulations have been performed to study wave breaking [13, 14, 15, 16], much less attention was paid to the wind turbulence over breaking waves. The numerical methods for simulating flows with a wave surface can be categorized into one-fluid and two-fluids simulations. The one-fluid simulation has been successfully used to study airflow over prescribed non-breaking waves [17, 18, 19]. In these one-fluid simulations, the waves act as a bottom boundary with prescribed motions. In two-fluids simulations, the air and water are treated as a coherent system, with an interface-capturing technique, which includes but is not limited to the level-set (LS) method [20], volume-of-fluid (VOF) method [21], and coupled LS and VOF (CLSVOF) method [22].

In the present study, we perform DNS of turbulent wind over breaking waves with the breaking process resolved explicitly. The objective is to study the effect of wave breaking on the momentum and energy transfer in the airflow. We simulate air and water as a coherent system on Eulerian grid. The air–water interface is captured using the CLSVOF method. Because wave breaking is an unsteady process, time averaging is inappropriate to define turbulence statistics. Instead, we conduct 100 ensemble runs to calculate turbulence statistics based on ensemble averaging over these runs. Different runs have the same initial wind profile and wave geometry, but different instantaneous turbulence fluctuations.

Fig. 6 shows the computational domain and coordinates used in the present simulations. The streamwise, spanwise, and vertical directions are denoted by x , y , and z , respectively, and the corresponding velocity components are represented by u , v , and w , respectively. The wave propagates in the $+x$ -direction. The computational domain size is set to $L_x \times L_y \times L_z = 2\lambda \times 1.5\lambda \times 2.5\lambda$, where λ is the wave length of the primary wave studied (Fig. 6). The mean water depth d and air height h are 0.5λ and 2λ , respectively. The number of grid points used in the simulations is $N_x \times N_y \times N_z = 320 \times 192 \times 360$. In the x - and y -directions, the grid is evenly-spaced. In the z -direction, the grid is clustered between $z = -0.1\lambda$ and $z = 0.15\lambda$ with a fine and constant resolution of $\Delta_z = 0.002\lambda$, and the grid is stretched to the top of air and bottom of water. The initial wave steepness is $ka_0 = 0.55$, where $k = 2\pi/\lambda$ is the wave number, and a_0 is the initial wave amplitude. The wave age c/u_* is 3.7, where c is the wave phase speed, and u_* is the frictional velocity in the air. The Reynolds number is set to $Re = u_*\lambda/\nu = 180$ to perform DNS, where ν is the kinematic viscosity.

Fig. 7 shows the vertical profiles of the plane-averaged mean streamwise velocity $\langle u \rangle$, Reynolds shear stress $-\langle u'w' \rangle$, turbulent kinetic energy (TKE) $k_{pl} = (\langle u'u' \rangle + \langle v'v' \rangle + \langle w'w' \rangle)/2$, and TKE production $P_k = -\langle u'w' \rangle d\langle u \rangle/dz$ before ($t = 0.0T$), during ($t = 0.8T$), and after ($t = 3.0T$) wave plunging. Here, the angular bracket defines the averaging

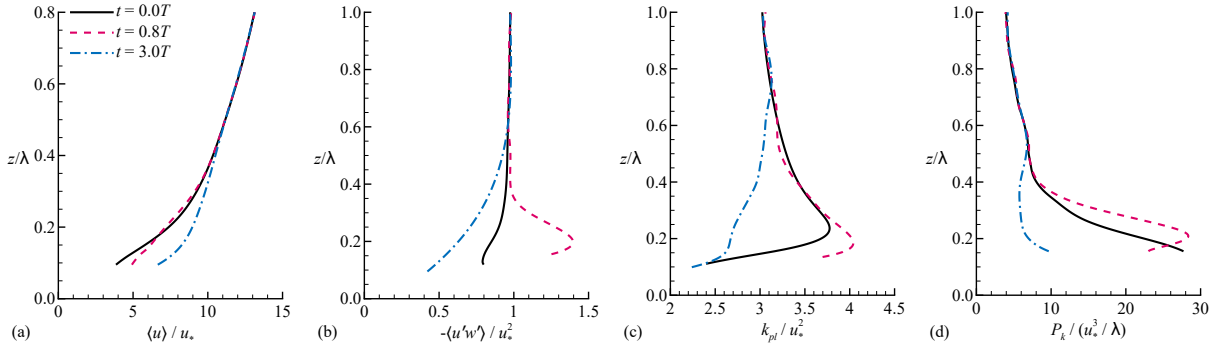


Fig. 7. Vertical profiles of (a) plane-averaged mean streamwise velocity $\langle u \rangle / u_*$, (b) Reynolds shear stress $-\langle u'w' \rangle / u_*^2$, (c) TKE k / u_*^2 , and (d) TKE production $P_k / (u_*^3 / h)$ at different stages of wave plunging.

ing in horizontal plane and ensembles, and the prime denotes the corresponding turbulence fluctuations. All profiles in the figure are nondimensionalized using u_* and h as the characteristic velocity and length scales, respectively.

It can be observed from Fig. 7(a) that the magnitude of $\langle u \rangle$ near the wave surface is larger at $t = 3.0T$ than at $t = 0.0T$, indicating the overall transport of momentum from water to air during the wave plunging. However, $\langle u \rangle$ experiences a transient decrease above $z/\lambda = 0.18$ before $t = 0.8T$. The plane-averaged Reynolds shear stress $-\langle u'w' \rangle$ plays an important role in the evolution of the plane-averaged mean streamwise velocity $\langle u \rangle$, of which the governing equation reads

$$\frac{\partial \langle u \rangle}{\partial t} = \nu \frac{\partial^2 \langle u \rangle}{\partial z^2} - \frac{\partial \langle u'w' \rangle}{\partial z} \quad (5)$$

Fig. 7(b) shows that the first plunging event disturbs the air near the wave surface. As a result, there exists a peak in the profile of $-\langle u'w' \rangle$ near $z/\lambda = 0.2$ at $t = 0.8T$. Below and above this peak, the value of $-\partial \langle u'w' \rangle / \partial z$ is positive and negative, respectively. Because the viscous shear stress is less important than the Reynolds shear stress in this region, it is understood from equation (5) that during wave breaking, the wind speed $\langle u \rangle$ is accelerated and decelerated below and above the peak of $-\langle u'w' \rangle$, respectively. The peak of $-\langle u'w' \rangle$ moves upward with its magnitude decreasing after $t = 0.8T$, leading to an expansion of the acceleration region. As a result, the mean velocity increases after $t = 0.8T$ (Fig. 7a).

The wave plunging also influences the TKE k_{pl} near the wave surface significantly. As shown in Fig. 7(c), the value of k_{pl} below $z/\lambda = 0.35$ is higher at $t = 0.8T$ than at $t = 0.0T$, indicating that the turbulence is transiently enhanced due to the wave breaking. The magnitude of k_{pk} is smaller at $t = 3.0T$ than at $t = 0.0T$, indicating that the turbulence is eventually reduced after wave plunging ceases.

To further study why the transient growth of TKE takes place, we compare the production of TKE, P_k . It is evident from Fig. 7(d) that the magnitude of P_k is larger at $t = 0.8T$ than at $t = 0.0T$. From the expression of P_k , it is known that the value of P_k is determined by the vertical gradient of mean velocity $\partial \langle u \rangle / \partial z$ and the Reynolds shear stress $-\langle u'w' \rangle$. Fig. 7(a) shows that $\partial \langle u \rangle / \partial z$ decreases during the first plunging event, which tends to reduce the value of P_k . In contrast, as shown in Fig. 7(b), the magnitude of $-\langle u'w' \rangle$ increases and a peak occurs in its profile due to the disturbance effect of the wave breaking on the turbulent flow, which tends to cause an increase of P_k . Fig. 7(d) indicates that the latter effect is stronger, and as a result k_{pl} experiences a transient growth during the first plunging event (Fig. 7c).

Next, we study the wave-phase-averaged airflow statistics. Fig. 8 shows the phase-averaged mean streamwise velocity \bar{u} , mean vertical velocity \bar{w} , and mean spanwise vorticity $\bar{\omega}_y$ near the wave surface during the wave plunging at $t = 0.8T$. Here, the bar denotes the averaging in spanwise direction, wave phase, and ensembles. The instantaneous wave surface varies with the spanwise coordinate y . Moreover, it differs among different ensemble runs. Therefore, the air–water interfaces should not be represented deterministically by a single line in a 2D plot of phase-averaged statistics. We use a thick dash-dotted line to denote the upper bound of all interfaces.

As shown in Fig. 8(a), when the overturning jet impinges onto the wave surface, it pushes the air to move forward. This process accelerates the airflow in the streamwise direction, and as a result, a high-speed region is formed ahead

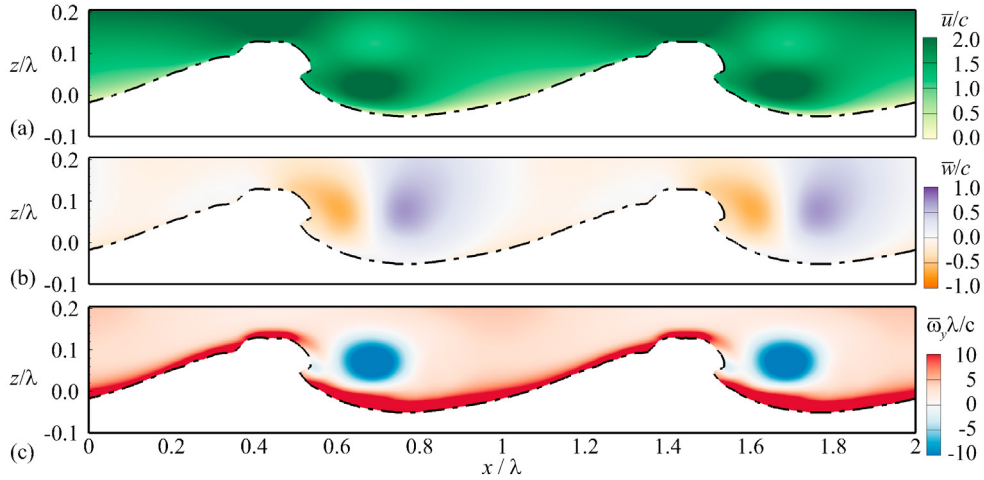


Fig. 8. Phase-averaged flow field at $t = 0.8T$. (a) Mean streamwise velocity \bar{u} , (b) mean vertical velocity \bar{w} , and (c) mean spanwise vorticity $\bar{\omega}_y$. The dash-dotted line represents the upper bound of all wave surfaces, defined as the isopleth of $\tilde{\psi} = 0.05$, where ψ is the volume fraction of water. Note that the upper bound of wave surface is different from the instantaneous wave surface, which can be represents by the isopleth of $\psi = 0.5$. The wave propagates in the $+x$ -direction.

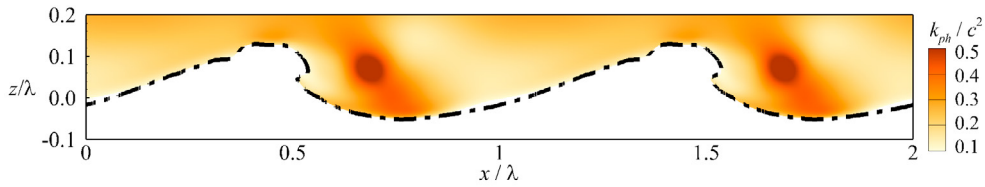


Fig. 9. Contours of phase-averaged TKE k_{ph}/c^2 at $t = 0.8T$. The thick dashed-dotted line represents the top bound of wave surfaces. The waves propagate in the $+x$ -direction.

of the wave front. Meanwhile, the jet brings the air particles around it to impinge onto the wave surface. Therefore, the vertical velocity of airflow is negative on the leeward of the wave crest (Fig. 8b). The airflow above the vortex is decelerated to compensate the air moving downward with the jet, such that a low-speed region appears above the vortex (Fig. 8a). A counterclockwise-rotating vortex is generated during wave plunging. This vortex corresponds to the negative vorticity in Fig. 8(c).

Fig. 9 displays the contours of the phase-averaged TKE $k_{ph} = (\overline{u''u''} + \overline{v''v''} + \overline{w''w''})/2$ near the wave surface at $t = 0.8T$. Here, the double prime denotes the fluctuations with respect to the phase averaging. As shown, the magnitude of k_{ph} is large near the spanwise vortex shown in Fig. 8(c), indicating that the turbulence is enhanced by the vortex. This is consistent with the result of the plane-averaged TKE shown in Fig. 7(c).

4. Wind over Broad-Band Waves

In this section, we study wind turbulence over broad-band waves following [35, 36], where the wind field is simulated using LES and the wave evolution is computed using a high-order spectral method [23]. The physical and numerical parameters of the simulation are listed in Table 4. An instantaneous wind field, as denoted by the streamwise velocity in an $x - z$ plane, and a wave field, as denoted by the surface elevation, are plotted in Fig. 10.

We first examine the wind turbulence above the water from the perspective of space–time correlation. The full wavenumber–frequency spectrum of the streamwise velocity [28] is calculated and plotted in Fig. 11. For the purpose of clarity and to simplify the analysis, the spectrum $F_{11}(k_1, k_2, \omega)$ is projected onto the spectral plane (k_1, ω) . Fig. 11 shows that the shape of the spectrum is a combined result of different effects caused by the mean flow, large turbulence eddies, and waves. Consider the turbulence motion on a horizontal plane, the convection due to the mean flow $U(z)$

Table 4. Parameters of the wind and wave simulations. Here, L_x , L_y , and L_z are the computational domain size in three directions, N_x , N_y , and N_z are the grid number correspondingly, u_* is the friction velocity, U_{10} is the initial wind speed at 10m above the mean water surface, α_p is the Phillips parameter of the initial JONSWAP spectrum, and $f_{p,0}$ is the initial peak wave frequency.

Simulation	(L_x, L_y, L_z) (m)	$(N_x \times N_y \times N_z)$ (wind) / $(N_x \times N_y)$ (wave)	u_* (m/s)	U_{10} (m/s)	α_p	$f_{p,0}$ (Hz)
Wind field (LES)	200, 100, 100	$256 \times 128 \times 256$	0.22	6	—	—
Wave field (HOS)	200, 100	512×256	—	—	0.0144	0.40

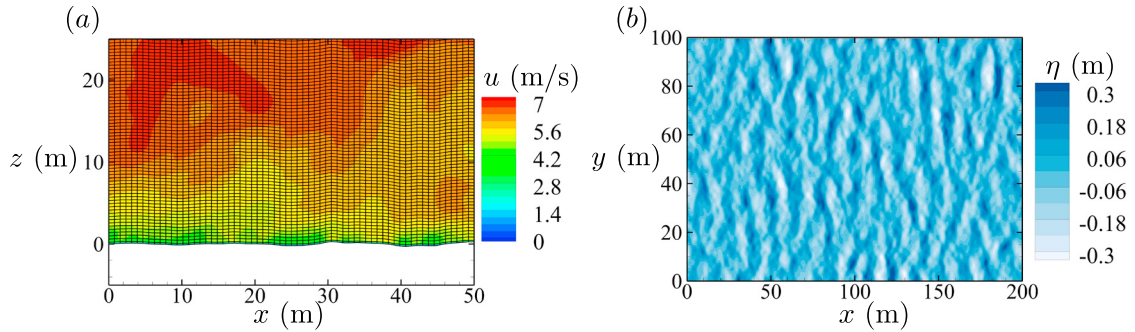


Fig. 10. A snapshot of the contours of the instantaneous (a) wind streamwise velocity u in an $x-z$ plane, and (b) wave surface elevation η . Also plotted in (a) is the wave-boundary-fitted grid in the wind simulation. Only part of the wind field is plotted for clarity.

causes a change in the frequency of turbulence motions, and turns a spatial oscillation into a temporal one, which can be seen from the “frozen turbulence hypothesis” [30]. Large energy-containing eddies lead to a broadening of the spectrum, which can be theoretically explained by the random-sweeping model of the spectrum [33, 34]. Besides these two features related to the Doppler effect, a unique wave signature is found in the spectrum, which is identified by another branch along the dispersion relation of gravity waves $\omega = \sqrt{gk_1}$. It is evident that the wave-induced energy is significant for a wide range of motions of different scales, especially in the high wavenumber region. This discovery can be used as a measure of the wave effect on the wind turbulence.

We next investigate nonlinear wave interactions, a key process in wave field evolution. Here, the nonlinear wave interactions refer to the energy transfer among four wave components, which is quantified by the Hasselmann equation [24, 25, 26]:

$$S_{nl}(\mathbf{k}_1) = \omega_4 \int Q(\mathbf{k}_1, \mathbf{k}_2, \mathbf{k}_3, \mathbf{k}_4) \delta(\mathbf{k}_1 + \mathbf{k}_2 - \mathbf{k}_3 - \mathbf{k}_4) \delta(\omega_1 + \omega_2 - \omega_3 - \omega_4) [n_1 n_2 (n_3 + n_4) - n_3 n_4 (n_1 + n_2)] d\mathbf{k}_2 d\mathbf{k}_3, \quad (6)$$

where S_{nl} is the rate of change of the wave energy caused by four-wave interaction, ω_i is the angular frequency of a wave component, $n_i(\mathbf{k}_i) = E(\mathbf{k}_i)/\omega_i$ is the ratio of wave energy density function $E(\mathbf{k}_i)$ to wave frequency, i.e., the wave action density function, and $Q(\mathbf{k}_1, \mathbf{k}_2, \mathbf{k}_3, \mathbf{k}_4)$ is a complex function of wavenumber vectors.

We calculate the exact four-wave interaction of the initial spectrum by integrating the Hasselmann equation using two different methods: the quadrature method [27] and the Webb-Resio-Tracy (WRT) method [32, 31]. The results are shown in Fig. 12. While there are some discrepancies because of the different numerical approaches used in the two methods, the main features of the nonlinear interactions are captured as expected [37]. Most notably, there is a change of sign in the value of S_{nl} near the peak $f/f_{p,0}$, suggesting the energy transfer from higher wavenumber components to lower wavenumber ones, resulting in the frequency downshift. This phenomenon is observed in the coupled wind-wave simulation as shown in Fig. 13(a), where the wave peak moves to the lower frequency region near $f = 0.8f_{p,0}$ after an evolution period of $t \approx 3600T_{p,0}$. To further investigate the role four-wave interaction plays in this process, we calculate the rate of change of the omnidirectional frequency spectrum $\Delta E/\Delta t$ using the simulation data of the wind-forced wave field, and compare it with S_{nl} . The results are presented in Fig. 13(b). Here, the exact solutions of omnidirectional S_{nl} are directly calculated from the directional result by integration over the coordinate θ (see Fig. 12), while the numerical solution of S_{nl} is calculated from an independent HOS simulation following [29]. We find that

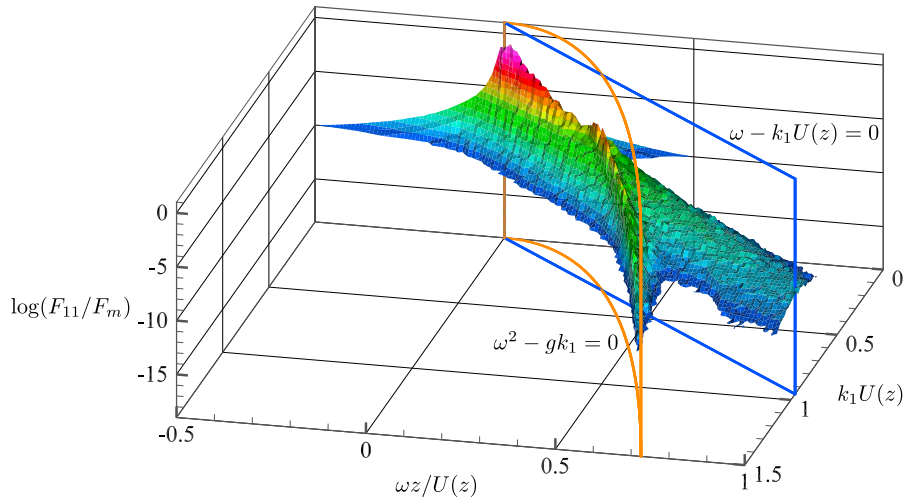


Fig. 11. Wavenumber–frequency spectrum of the streamwise velocity of the wind field. The spectrum is normalized by its maximum value F_m . The raw data used for analysis is from the horizontal plane $z = 1.2\text{m}$ above the mean water surface. Also plotted are two surfaces denoting the Doppler shift $\omega = k_1 U(z)$ and the dispersion relation of deep water wave $\omega = \sqrt{gk_1}$.

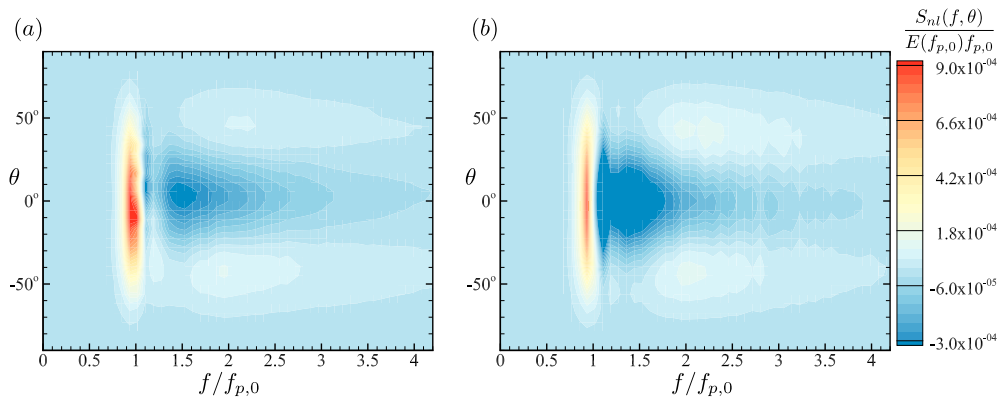


Fig. 12. Four-wave interaction-induced energy transfer $S_{nl}(f, \theta)$ calculated using (a) the quadrature method and (b) the WRT method, normalized by the peak frequency $f_{p,0}$ and the energy density function $E(f_{p,0})$ of the initial wave field.

the shape of the total energy transfer is similar to that of the four-wave interaction term, exhibiting a change of sign. Compared with wind input, four-wave interaction has no net energy contribution to the wave field since it is an internal energy redistribution mechanism among wave components. However, our numerical result shows that the strength of four-wave interaction dominates over wind input locally in the spectral space. Therefore, the four-wave interaction may serve as the dominant mechanism that determines the wave spectrum shape and thus plays an important role in the long-term evolution of wave fields.

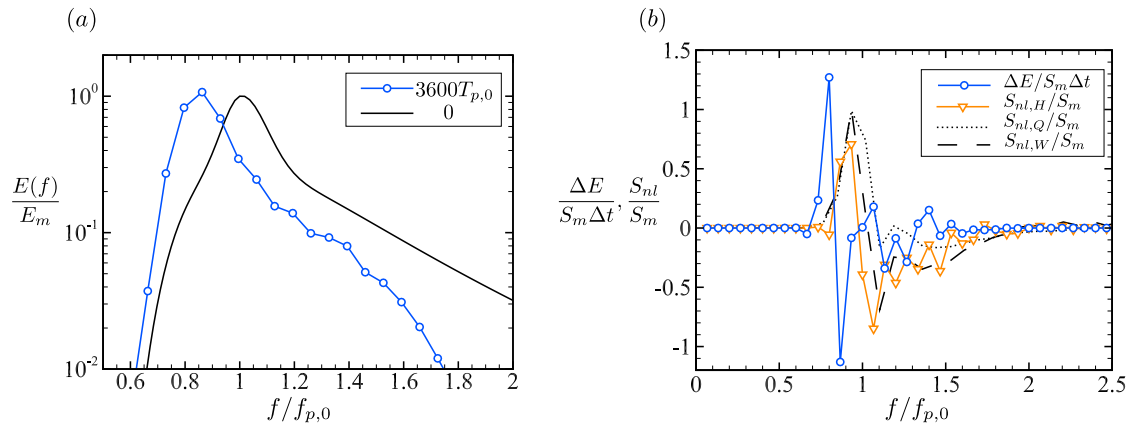


Fig. 13. Normalized omnidirectional wave spectrum (a), and rate of change of the spectrum (b), at $t \approx 3600T_{p,0}$. In (a), the black solid line denotes the initial JONSWAP spectrum, where E_m is its maximum value. Also plotted in (b) are the nonlinear interaction terms based on the initial spectrum calculated using the quadrature method $S_{nl,Q}$, the WRT method $S_{nl,W}$, and the HOS simulation data $S_{nl,H}$. Here, S_m denotes the maximum value of the WRT result.

5. Conclusions

In this paper, we have presented numerical results of wind over different wave fields. In the first part, we use DNS to study wind over two progressive waves and investigate the sheltering effect of a long wave on a short wave. We find that in the presence of the long wave the form drag of the short wave decreases, with the magnitude of the reduction depending on the wave age, or equivalently the magnitude of the form drag on the long wave. The larger the magnitude of the form drag on the long wave, the stronger the sheltering effect, and thus the larger relative reduction of the form drag on the short wave. By calculating the correlation between the spatial distribution of streamwise vorticity and the surface friction on the surface waves, we have shown that the local reduction of the surface friction on the windward face of the long wave by the presence of the short wave is correlated to the breaking of streamwise vortical structures. In the second part, we use DNS to study wind turbulence over breaking waves. It is found that wave plunging significantly influences the turbulence statistics near the wave surface. During the plunging, the air is accelerated in the streamwise direction due to the push of the overturning jet. The wave plunging also induces a large spanwise vortex. Near this vortex, the air is highly disturbed, and the magnitude of TKE increases significantly. Above the wave crest, the magnitude of TKE grows transiently during wave plunging. The investigation of TKE production shows that the transient growth of TKE results from a peak occurring in the profile of the Reynolds shear stress. Finally, we show the result of wind over broad-band waves, simulated using the coupled LES–HOS model. The wave signature on the wind turbulence is elucidated in the wavenumber–frequency spectrum of the streamwise wind velocity, indicating the significance of wave effect on the wave boundary layer. We also observe the frequency downshift phenomenon in the long-term evolution of the wave field. By comparing the total wave energy change and that caused by four-wave interaction, we show that four-wave interaction dominates the evolution of the wind-wave field.

Acknowledgements

The support to this research by ONR and NSF is gratefully acknowledged.

References

1. D. Yang, L. Shen, Simulation of viscous flows with undulatory boundaries. Part I: Basic solver, *Journal of Computational Physics*, 2011; **230** 5488–5509.
2. D. Yang, L. Shen, Direct-simulation-based study of turbulent flow over various waving boundaries, *Journal of Fluid Mechanics*, 2010; **650** 131–80.

3. O. M. Phillips, M. L. Banner, Wave breaking in the presence of wind drift and swell, *Journal of Fluid Mechanics*, 1974; **66** 625-640.
4. M. A. Donelan, The effect of swell on the growth of wind waves, *Johns Hopkins APL Technical Digest*, 1987; **8** 18-23.
5. G. Chen, S.E. Belcher, Effects of long waves on wind-generated waves, *Journal of Physical Oceanography*, 2000; **30** 2246-2256.
6. A. G. Kravchenko, H. Choi, P. Moin, On the relation of near-wall streamwise vortices to wall skin friction in turbulent boundary layers, *Physics of Fluids A: Fluid Dynamics*, 1993; **5** 3307-3309.
7. M. L. Banner, D. H. Peregrine, Wave breaking in deep water, *Annual Review of Fluid Mechanics*, 1993; **25** 373-97.
8. W. K. Melville, The role of surface-wave breaking in air-sea interaction, *Annual Review of Fluid Mechanics*, 1996; **28** 279-321.
9. M. Perlin, W. W. Schultz, Capillary effects on surface waves, *Annual Review of Fluid Mechanics*, 2000; **32** 241-74.
10. J. H. Duncan, Spilling breakers, *Annual Review of Fluid Mechanics*, 2000; **33** 519-47.
11. K. T. Kiger, J. H. Duncan, Air-entrainment mechanisms in plunging jets and breaking waves, *Annual Review of Fluid Mechanics*, 2012; **44** 563-96.
12. M. Perlin, W. Choi, Z. Tian, Breaking waves in deep and intermediate waters, *Annual Review of Fluid Mechanics*, 2013; **45** 115-45.
13. A. Iafraiti, Numerical study of the effects of the breaking intensity on wave breaking flows, *Journal of Fluid Mechanics*, 2009; **622** 371-411.
14. M. Derakhti, J. T. Kirby, Bubble entrainment and liquid-bubble interaction under unsteady breaking waves, *Journal of Fluid Mechanics*, 2014; **761** 464-506.
15. L. Deike, S. Popinet, W. K. Melville, Capillary effects on wave breaking, *Journal of Fluid Mechanics*, 2015; **769** 541-69.
16. P. Lubin, S. Glockner, Numerical simulations of three-dimensional plunging breaking waves: generation and evolution of aerated vortex filaments, *Journal of Fluid Mechanics*, 2015; **767** 364-93.
17. P. P. Sullivan, J. C. McWilliams, C.-H. Moeng, Simulation of turbulent flow over idealized water waves, *Journal of Fluid Mechanics*, 2000; **404** 47-85.
18. D. Yang, L. Shen, Direct-simulation-based study of turbulent flow over various waving boundaries, *Journal of Fluid Mechanics*, 2010; **650** 131-80.
19. T. Hara, P. P. Sullivan, Wave boundary layer turbulence over surface waves in a strongly forced condition, *Journal of Physics Oceanography*, 2015; **45** 868-83.
20. S. Osher, J. A. Sethian, Fronts propagating with curvature-dependent speed: algorithms based on Hamilton-Jacobi formulations, *Journal of Computational Physics*, 1988; **79** 12-49.
21. R. Scardovelli, S. Zaleski, Direct numerical simulation of free-surface and interfacial flow, *Annual Review of Fluid Mechanics*, 1999; **31** 567-603.
22. M. Sussman, E. G. Puckett, A coupled level set and volume-of-fluid method for computing 3D and axisymmetric incompressible two-phase flows, *Journal of Computational Physics*, 2000; **162** 301-37.
23. D. G. Dommermuth, D. K. P. Yue, A high-order spectral method for the study of nonlinear gravity waves, *Journal of Fluid Mechanics*, 1987; **184** 267-288.
24. K. Hasselmann, On the non-linear energy transfer in a gravity-wave spectrum. Part 1. General theory, *Journal of Fluid Mechanics*, 1962; **12** 481-500.
25. K. Hasselmann, On the non-linear energy transfer in a gravity-wave spectrum. Part 2. Conservation theorems; wave-particle analogy; irreversibility, *Journal of Fluid Mechanics*, 1963; **15** 273-281.
26. K. Hasselmann, On the non-linear energy transfer in a gravity-wave spectrum. Part 3. Evaluation of the energy flux and swell-sea interaction for a Neumann spectrum, *Journal of Fluid Mechanics*, 1963; **15** 385-398.
27. I. V. Lavrenov, Effect of wind wave parameter fluctuation on the nonlinear spectrum evolution, *Journal of Physical Oceanography*, 2001; **31** 861-873.
28. S. B. Pope, *Turbulent Flows*, 2000. Cambridge University Press, Cambridge; New York.
29. M. Tanaka, Verification of Hasselmann's energy transfer among surface gravity waves by direct numerical simulations of primitive equations, *Journal of Fluid Mechanics*, 2001; **444**, 199-221.
30. G. I. Taylor, The spectrum of turbulence, *Proceedings of the Royal Society A: Mathematical, Physical and Engineering Sciences*, 1938; **164**, 476-490.
31. B. A. Tracy, D. T. Resio, Theory and calculation of the nonlinear energy transfer between sea waves in deep water, *Technical Report*, 1982. Hydraulics Laboratory, U.S. Army Engineer Waterways Experiment Station. Vicksburg, Miss.
32. D. J. Webb, Non-linear transfers between sea waves, *Deep Sea Research*, 1978; **25**, 279-298.
33. M. Wilczek, Y. Narita, Wave-number-frequency spectrum for turbulence from a random sweeping hypothesis with mean flow, *Physical Review E - Statistical, Nonlinear, and Soft Matter Physics*, 2012; **86**, 1-8.
34. M. Wilczek, R. J. A. M. Stevens, Y. Narita, C. Meneveau, A wavenumber-frequency spectral model for atmospheric boundary layers, *Journal of Physics: Conference Series*, 2014; **524**, 012104.
35. D. Yang, C. Meneveau, L. Shen, Effect of downwind swells on offshore wind energy harvesting - A large-eddy simulation study, *Renewable Energy*, 2014; **70**, 11-23.
36. D. Yang, C. Meneveau, L. Shen, Large-eddy simulation of offshore wind farm, *Physics of Fluids*, 2014; **26**, 025101.
37. I. R. Young, *Wind Generated Ocean Waves*, 1999. Elsevier. Amsterdam; New York.